IEEE Robotics and Automation Letters (RA-L) paper, presented at ICRA 2026, Vienna, Austria. Cite as RA-L paper.

Data-driven Control Optimization on Frequency Response for Fast and Precise Motion of Flexible Joint Robots

Deokjin Lee, Junho Song, and Sehoon Oh

***Abstract*—This paper presents a data-driven control optimization framework for flexible joint robots (FJR) based on frequency response function (FRF) data, enabling automated controller synthesis without explicit model identification. Unlike conventional model-based approaches that rely on accurate parameter estimation, the proposed method directly utilizes measured FRF data and formulates the controller design as a convex optimization problem. The controller maximizes control bandwidth while ensuring stability across a wide range of configurations. Experimental validation on a FJR demonstrates superior tracking accuracy, vibration suppression, and robustness compared to model-based methods. Furthermore, a high-speed drumming task demonstrates the ability of the controller to handle repeated impacts and inertia variations, highlighting the potential of FRF-based control for the fast and precise operation of flexible robotic systems.**

***Index Terms*—Convex optimization, data-driven control, frequency response data, flexible joint robot, system variation**

I. Introduction

ROBOTS are increasingly being deployed in diverse human environments, extending their role beyond traditional labor replacement to applications such as healthcare, education, and entertainment [1]. As robotic systems become more integrated into human-centric settings, safety assurance, and effective human-robot interaction have emerged as critical research challenges [2]. Among various robotic architectures, flexible joint robots (FJR) have attracted considerable interest due to their inherent compliance and soft actuation, which facilitate safer and more adaptable interaction with uncertain environments [3].

Despite their advantages, FJRs pose significant challenges for motion control due to structural flexibility. This flexibility leads to reduced control bandwidth, low-frequency resonances, and degraded trajectory tracking accuracy [4], ultimately limiting achievable speed and motion precision, especially during dynamic tasks. Consequently, enhancing control bandwidth while preserving system stability remains a critical objective in improving FJR performance [5].

Manuscript received: JUNE 28 2025; Revised: SEPTEMBER 27 2025; Accepted: OCTOBER 31 2025.

This paper was recommended for publication by Editor Lucia Pallottino upon evaluation of the Associate Editor and Reviewers' comments. This work was supported by Basic Science Research Program through the National Research Foundation of Korea (NRF) funded by the Ministry of Education No. RS-2025-25420118 (*Deokjin Lee and Junho Song contributed equally to this work.*) (*Corresponding author: Sehoon Oh.*)

Deokjin Lee, Junho Song, and Sehoon Oh are with the Department of Robotics and Mechatronics Engineering, DGIST, Daegu, 42988, Republic of Korea (e-mail: djlee@dgist.ac.kr; optimus120@dgist.ac.kr; sehoon@dgist.ac.kr).

Digital Object Identifier (DOI): 10.1109/LRA.2025.3634887

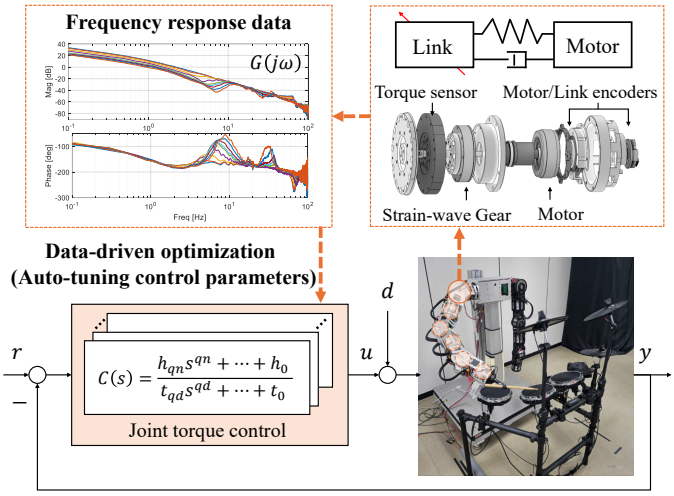

Fig. 1. Proposed auto-tuning control framework for flexible joint robots. Joint controllers are synthesized via convex optimization using frequency response data, improving bandwidth and robustness without requiring model identification.

To address these challenges, various robust control strategies have been proposed, including passivity-based control [6], $\mathcal{H}_\infty$ control [7], and disturbance observers [8]. These methods are effective in suppressing vibrations and enhancing disturbance rejection. However, they typically rely on accurate dynamic models, which are difficult to obtain due to nonlinearities, parameter uncertainties, and sensitivity to measurement noise.

System identification based on frequency response function (FRF) is widely employed to characterize robot dynamics in the frequency domain [9]–[11]. FRF provides valuable insight into the resonant behavior of the system and serves as a useful foundation for control design. Nonetheless, constructing an accurate FRF-based model requires careful excitation, noise attenuation, and parameter fitting, which remain nontrivial challenges [12]. Furthermore, traditional FRF-based controller design often relies on expert-driven manual tuning, limiting its automation potential and scalability.

Data-driven control synthesis that directly utilizes measured FRF data without explicit model identification has been proposed in [13]. This approach is particularly advantageous for FJRs, where accurate modeling is complicated by configuration-dependent resonance and anti-resonance modes, unlike rigid joint robots. However, the method neither explicitly addresses control bandwidth maximization nor formulates the problem in the joint space, which is the fundamental coordinate framework for robotic systems. Moreover, although an FRF-based optimization framework for bandwidth maximization is introduced in [14], it remains restricted to single-

IEEE Robotics and Automation Letters (RA-L) paper, presented at ICRA 2026, Vienna, Austria. Cite as RA-L paper.

input single-output (SISO) systems and thus cannot capture the dynamic variations inherent in multi-joint robots.

To address these limitations, this paper proposes a novel FRF-based data-driven optimization framework for controller synthesis in FJRs as illustrated in Fig. 1. The proposed method aims to maximize control bandwidth while ensuring closed-loop stability across varying operating conditions. The key contributions of this work are as follows:

- The use of measured FRF data enables accurate characterization of FJR dynamics, capturing nonlinear effects such as friction without requiring explicit model parameterization.
- An optimization-based framework is developed to automatically tune control parameters using FRF data, allowing adaptation to configuration-dependent system behavior.
- The control bandwidth is maximized through an optimization process that ensures closed-loop stability and is experimentally validated on multi-joint robotic systems performing a high-speed drumming task.

The structure of the paper is as follows: Section II discusses the challenges associated with motion control for FJRs. Section III presents the optimization methodology, which leads to a non-convex problem formulation for motion control of FJRs. Section IV then addresses the convexification of the proposed non-convex formulation. Section V validates the proposed controller through experiments. Finally, Section VI concludes the paper.

II. Problem Definition

A. Challenges in High-Speed Control of Flexible Joint Robots

FJRs can be modeled and controlled using a SISO framework at the joint level. The joint dynamics typically exhibit a combination of rigid-body and flexible modes. A generalized transfer function capturing the joint dynamics with N_r modes—including one rigid body mode and $N_r - 1$ flexible modes—can be described as [15]:

$$G(s) = \frac{1}{Js^2 + Bs} \prod_{k=1}^{N_r-1} \frac{s^2 + 2\eta_{a,k}\omega_{a,k}s + \omega_{a,k}^2}{s^2 + 2\eta_{n,k}\omega_{n,k}s + \omega_{n,k}^2}, \tag{1}$$

where J and B denote the joint inertia and damping coefficient, respectively. The parameters $\eta_{(\cdot),k}$ and $\omega_{(\cdot),k}$ represent the damping ratio and natural frequency of the k-th flexible mode, with subscripts n and a indicating resonance and anti-resonance, respectively. As the number of flexible modes increases, control design becomes more challenging due to the multiple resonances and associated phase lags, which limit the achievable control bandwidth.

1) Configuration-Dependent Flexibility and Inertia Variation: FJRs exhibit structural compliance at each joint, which introduces resonance phenomena and vibration during motion. These resonances are highly configuration-dependent because the reflected link inertia varies significantly with the robot posture. Consequently, as the robot transitions across different configurations, the resonance frequencies shift, as illustrated in Fig. 2, making consistent control more difficult. A controller tuned for one configuration becomes suboptimal—or even unstable—when applied to another. In addition, multi-joint coordination introduces coupling effects that can amplify vibration and further degrade trajectory accuracy. These challenges are particularly pronounced in high-speed or dynamically reconfiguring tasks, where maintaining stable and accurate performance across a wide range of operating conditions is essential.

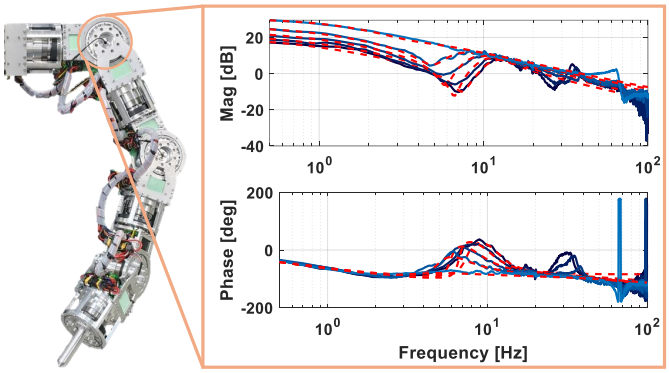

Fig. 2. Challenges in accurate model identification for flexible joint robots. Solid lines depict position-dependent FRF data at different robot configurations, while dashed lines represent identified models. These models have limited capacity to capture configuration-dependent variations, highlighting the limitations of conventional model-based control.

2) Vulnerability to Modeling Errors and Uncertainties: Conventional model-based control approaches depend on accurate knowledge of the dynamic parameters of the system. However, for FJRs, modeling errors frequently arise due to joint friction, unmodeled dynamics, and parameter uncertainties as shown in Fig. 2. The flexible elements introduce complex vibrational behavior that is difficult to capture analytically. Even with FRF data, model fitting requires selecting appropriate structures and parameters, which may not generalize well across varying operating conditions. These inaccuracies constrain the performance of model-based controllers and hinder real-time adaptation without extensive expert tuning.

3) Limited Control Bandwidth: The presence of flexible modes significantly limits the achievable control bandwidth of FJRs. Attempts to increase bandwidth without properly addressing these resonances may lead to instability or excessive vibration. Traditional approaches adopt conservative bandwidth margins to ensure robustness, resulting in slow system responses. This limitation becomes a major bottleneck in high-speed applications such as dynamic manipulation, where precise and rapid motion tracking is essential. Therefore, advanced control strategies are required to extend the bandwidth while preserving stability in the presence of structural flexibility.

B. Frequency Response Data-Driven Control

To overcome the limitations of conventional model-based control approaches, a data-driven methodology that directly utilizes FRF data is proposed, thereby eliminating the need for explicit dynamic model identification. The FRF of the FJR system is defined as:

$$G(j\omega) = \frac{Y(j\omega)}{U(j\omega)}, \tag{2}$$

IEEE Robotics and Automation Letters (RA-L) paper, presented at ICRA 2026, Vienna, Austria. Cite as RA-L paper.

where $U(j\omega)$ and $Y(j\omega)$ denote the Fourier transforms of the input and output signals, respectively. Here, $j = \sqrt{-1}$ is the imaginary unit, and $\omega \in \Omega := (0, \pi/T_s]$, with T_s representing the sampling period.

Rather than constructing a model of the system, the controller is directly parameterized as a rational transfer function:

$$C(s) = \frac{h_{qn}s^{qn} + ... + h_0}{t_{qd}s^{qd} + ... + t_0}, \tag{3}$$

where $h = [h_{qn}, \ldots, h_0]^T$ and $t = [t_{qd}, \ldots, t_0]^T$ represent the controller coefficients to be optimized. The orders of the numerator and denominator, qn and qd, are chosen by the designer based on performance and complexity considerations.

Given the FRF data and the specified controller structure, the closed-loop characteristics are defined as:

$$L(j\omega, h, t) = G(j\omega)C(j\omega) = \frac{N(j\omega, h)}{D(j\omega, t)}, \tag{4}$$

$$S(j\omega, h, t) = \frac{D(j\omega, t)}{D(j\omega, t) + N(j\omega, h)}, \tag{5}$$

$$T(j\omega, h, t) = 1 - S(j\omega, h, t), \tag{6}$$

$$U(j\omega, h, t) = C(j\omega, h, t)S(j\omega, h, t). \tag{7}$$

These closed-loop functions—loop gain L, sensitivity S, complementary sensitivity T, and input sensitivity U—are computed directly from the measured FRF data and the candidate controller.

In the proposed framework, controller synthesis is formulated as a convex optimization problem, wherein the controller parameters h and t are optimized to maximize control bandwidth while satisfying performance and stability constraints. This formulation allows direct incorporation of frequency-domain specifications without relying on uncertain parametric models and inherently accounts for configuration-dependent dynamics, making it particularly well-suited for FJRs operating under variable conditions.

III. Optimization-based Controller Synthesis for Flexible Joint Robots

This section presents a FRF-based optimization framework that addresses the challenges identified in Section II-B, incorporating configuration-dependent dynamics, bandwidth maximization, and stability requirements into a unified framework.

A. Nyquist-Based Stability Margin Constraints

To ensure stability margins in the control design, the Nyquist plot must remain within the prescribed stability margin. This condition is enforced by satisfying the desired gain margin, g_m, and phase margin, ϕ_m [16]:

$$\sigma = \frac{g_m^2 - 1}{2g_m(g_m \cos\phi_m - 1)}, \tag{8}$$

$$r_m = \frac{(g_m - 1)^2 + 2g_m(1 - \cos\phi_m)}{2g_m(g_m \cos\phi_m - 1)}, \tag{9}$$

where σ and r_m denote the center and radius of the corresponding stability margin circle in the Nyquist plot, as illustrated in Fig. 3. The constraint to ensure stability becomes:

$$|\sigma + L(j\omega, h, t)| \geq r_m \qquad \forall\omega \in \Omega, \tag{10}$$

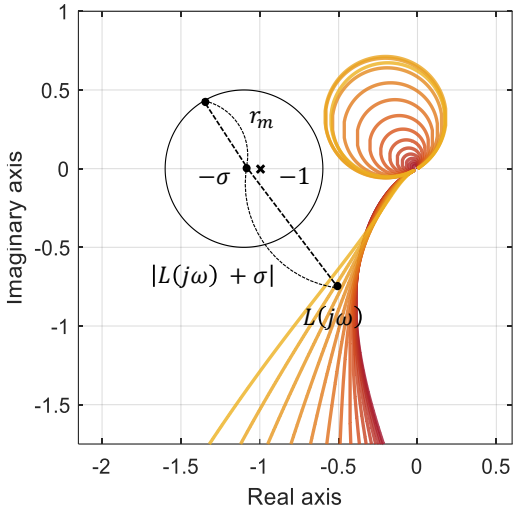

Fig. 3. Nyquist criterion illustrating the stability margin constraint for the flexible joint robot. Curves correspond to different robot configurations, with darker shades indicating larger link inertia

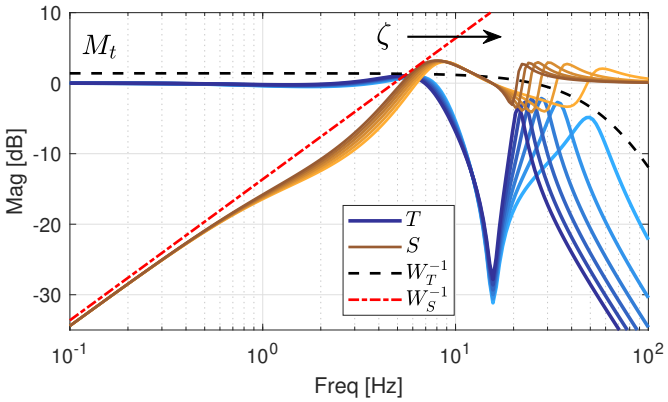

Fig. 4. Sensitivity and complementary sensitivity functions of the flexible joint robot across multiple configurations. Lighter to darker shades represent increasing link inertia. The controller preserves desired-loop shaping performance despite configuration-dependent dynamics.

where the conditions $0 < r_m < \sigma$ and $(\sigma - 1)^2 < r_m$ should hold. These conditions ensure that the control system remains stable by enclosing the critical point $(-1, j0)$ while excluding the origin.

B. Frequency-Domain Performance Constraints

Control performance is evaluated using three closed-loop transfer functions: the sensitivity function S, which characterizes disturbance rejection; the complementary sensitivity function T, which reflects tracking performance; and the input sensitivity function U, which relates to input constraints [17]. The corresponding performance specifications are defined by the following frequency-domain inequalities:

$$|W_S(j\omega, \zeta)S(j\omega, h, t)| \leq 1 \qquad \forall\omega \in \Omega, \tag{11}$$

$$|W_T(j\omega)T(j\omega, h, t)| \leq 1 \qquad \forall\omega \in \Omega, \tag{12}$$

$$|W_U U(j\omega, h, t)| \leq 1 \qquad \forall\omega \in \Omega, \tag{13}$$

where W_S, W_T, and W_U are frequency-dependent weighting functions that shape performance specifications over the

IEEE Robotics and Automation Letters (RA-L) paper, presented at ICRA 2026, Vienna, Austria. Cite as RA-L paper.

frequency range Ω. The weighting functions are defined as:

$$W_S(j\omega,\zeta) = \frac{\zeta}{j\omega}, \tag{14}$$

$$W_T(j\omega) = M_t^{-1}(\tau(j\omega)+1)^n, \tag{15}$$

$$W_U = \alpha. \tag{16}$$

Here, ζ represents the crossover frequency of the sensitivity function S. Increasing ζ shifts the sensitivity crossover toward higher frequencies, thereby raising the -3 dB cutoff frequency of the complementary sensitivity function T, which defines the closed-loop control bandwidth, as illustrated in Fig. 4. The weighting function W_T incorporates an nth-order low-pass filter, with M_t defining an upper bound on T, while α specifies the input constraint to prevent actuator saturation. The parameters n, M_t, and α are selected according to system requirements.

C. Optimization Problem Formulation

The controller synthesis problem is formulated as an optimization problem that maximizes the control bandwidth through the objective function ζ:

$$\underset{h,\,t}{\text{maximize}} \quad \zeta \tag{17a}$$

$$\text{subject to} \quad 0 < \zeta < \tau^{-n},\ 0 < h,\ t, \tag{17b}$$

$$|L(\omega,h,t)+\sigma| \geq r_m \qquad \forall\omega\in\Omega, \tag{17c}$$

$$|W_S(\omega,\zeta)S(j\omega,h,t)| \leq 1 \qquad \forall\omega\in\Omega, \tag{17d}$$

$$|W_T(\omega)T(j\omega,h,t)| \leq 1 \qquad \forall\omega\in\Omega, \tag{17e}$$

$$|W_U U(j\omega,h,t)| \leq 1 \qquad \forall\omega\in\Omega. \tag{17f}$$

This proposed formulation enables the controller to adapt to configuration-dependent variations while ensuring stability and maximizing performance across a wide range of operating conditions in FJRs. The following section presents the convexification of this non-convex problem formulation.

IV. Convex Reformulation for Controller Optimization

In this section, we propose a convex reformulation of the non-convex optimization problem introduced in Section III, employing linear matrix inequality (LMI) techniques [17] and suitable linear approximations.

A. Constraints for Stability Margin

The non-convex stability constraint from (17c) can be rewritten using the numerator N and denominator D of L as defined in (5). The subscript c indicates previously iterated values. The original non-convex stability margin inequality is expressed as:

$$|L(j\omega,h,t)+\sigma| - r_m \geq 0, \tag{18}$$

This condition can be reformulated as a convex-concave optimization problem [18]

$$|GN + D\sigma| \geq r_m|D|. \tag{19}$$

By applying a first-order Taylor expansion, the left-hand side is linearized as:

$$\Psi = F_c + \nabla F_c \begin{bmatrix} h-h_c \\ t-t_c \end{bmatrix}, \tag{20}$$

where $F = |G(j\omega)N(j\omega,h) + D(j\omega,t)\sigma|$. Thus, the inequality can be rewritten in affine form as:

$$\Psi \geq r_m|D|. \tag{21}$$

B. Constraints for Sensitivity Function

The sensitivity constraint in (17d):

$$|W_S(j\omega,\zeta)S(j\omega,h,t)| \leq 1, \tag{22}$$

can be reformulated using (14) and (6):

$$\left|\frac{\zeta}{j\omega}\right|^2 |D|^2 \leq P, \tag{23}$$

where $P = |D+GN|^2$. Since $|\zeta D|^2$ is not affine, the inequality does not satisfy convexity. Therefore, an additional inequality for γ can be derived using the Schur complement [17]:

$$\begin{bmatrix} 2\zeta_c^2 - \gamma\zeta_c^4 & \zeta \\ \zeta & 1 \end{bmatrix} \geq 0, \tag{24}$$

where $0 < \gamma < 2\zeta_c^{-2} - \zeta_c^{-4}\zeta^2 < \zeta^{-2}$. This yields the equivalent condition:

$$\left|\frac{\zeta}{\omega}\right|^2 |D(j\omega,t)|^2 \leq \frac{|D(j\omega,t)|^2}{|\omega|^2\gamma} \leq P(j\omega,h,t). \tag{25}$$

By substituting P with the linear approximation Φ as in (20),

$$|D|^2 \leq \omega^2\gamma\Phi. \tag{26}$$

Thus, the nonlinear constraint in (17d) is transformed into the following LMI condition:

$$\begin{bmatrix} \Phi & D(j\omega,t) \\ D(j\omega,t)^* & \omega^2\gamma \end{bmatrix} \geq 0. \tag{27}$$

C. Constraints for Complementary Sensitivity Function

Similar to IV-B, the complementary sensitivity function constraint in (17e)

$$|W_T(j\omega)T(j\omega,h,t)| \leq 1, \tag{28}$$

can be reformulated as with linear approximation in (20):

$$|M_t^{-1}Y|^2 \leq \Phi, \tag{29}$$

where $Y = |(\tau(j\omega)+1)^n GN|$. The nonlinear constraint in (17e) is thus reformulated as:

$$\begin{bmatrix} \Phi & M_t^{-1}Y(j\omega,h) \\ M_t^{-1}Y(j\omega,h)^* & 1 \end{bmatrix} \geq 0. \tag{30}$$

D. Constraints for Input Sensitivity Function

Similar to IV-B, the input sensitivity constraint in (17f)

$$|W_U U(j\omega,h,t)| \leq 1, \tag{31}$$

can be reformulated as:

$$|\alpha N|^2 \leq \Phi. \tag{32}$$

Thus, the nonlinear constraint (17f) can be reformulated as:

$$\begin{bmatrix} \Phi & \alpha N(j\omega,h) \\ \alpha N(j\omega,h)^* & 1 \end{bmatrix} \geq 0. \tag{33}$$

IEEE Robotics and Automation Letters (RA-L) paper, presented at ICRA 2026, Vienna, Austria. Cite as RA-L paper.

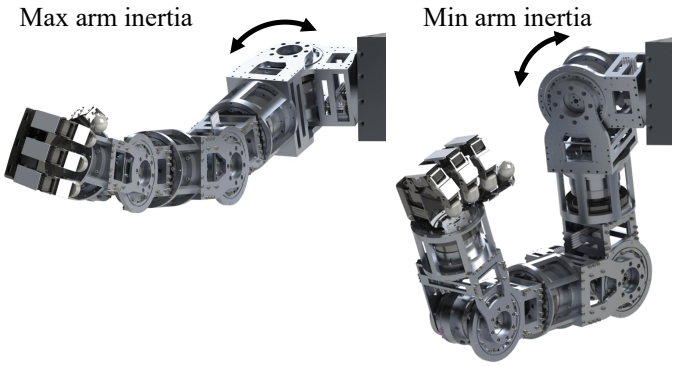

Fig. 5. Significant link inertia variation across different robot configurations.

TABLE I
REFLECTED LINK INERTIA ESTIMATED FROM CAD SOFTWARE.

Joint	Reflected Link Inertia (kg·m^2)		
	Min	Max	Variation (Max/Min)
1	0.03	3.98	124
2	0.01	4.15	415
3	0.014	0.69	49
4	0.50	0.70	1.4
5	0.008	0.09	11.3
6	0.07	–	–
7	0.0002	–	–

E. Convex Optimization Problem Formulation

The non-convex constraints of the optimization problem in Sec.III-C are transformed into convex constraints.

$$\underset{\tau,\, h}{\text{maximize}} \quad \zeta \tag{34a}$$

$$\text{subject to} \quad 0 < \zeta < \tau^{-n} \leq 1,\ 0 < \gamma,\ h,\ t, \tag{34b}$$

$$\Psi \geq r_m |D(j\omega, t)|, \tag{34c}$$

$$\begin{bmatrix} \Phi & D(j\omega,t) \\ D(j\omega,t)^* & \omega^2\gamma \end{bmatrix} \geq 0, \tag{34d}$$

$$\begin{bmatrix} 2\zeta_c^2 - \gamma\zeta_c^4 & \zeta \\ \zeta & 1 \end{bmatrix} \geq 0, \tag{34e}$$

$$\begin{bmatrix} \Phi & M_t^{-1}Y(j\omega,h) \\ M_t^{-1}Y(j\omega,h)^* & 1 \end{bmatrix} \geq 0, \tag{34f}$$

$$\begin{bmatrix} \Phi & \alpha N(j\omega,h) \\ \alpha N(j\omega,h)^* & 1 \end{bmatrix} \geq 0, \tag{34g}$$

All constraints are applied for all frequencies $\omega \in \Omega$. This convex reformulation enables efficient controller synthesis using standard LMI solvers while ensuring robust performance across varying FJR configurations.

V. EXPERIMENTAL VALIDATION

The proposed FRF-based control optimization framework is experimentally validated on a 7-DOF FJR system [19]. FRF data are collected across multiple configurations to capture configuration-dependent dynamics, and joint-level controllers are synthesized accordingly.

A. Robot Platform and Evaluation Setup

1) Hardware Description: Experiments are conducted on a 7-DOF FJR system composed of motors, harmonic drives, torque sensors, and dual encoders at each joint. The robot is operated at a 1 kHz control rate using EtherCAT communication. Mechanical compliance primarily arises from the harmonic drives and torque sensor assemblies. Fig. 5 illustrates example configurations that induce large link inertia variations, particularly in joints 1–3, as detailed in Table I.

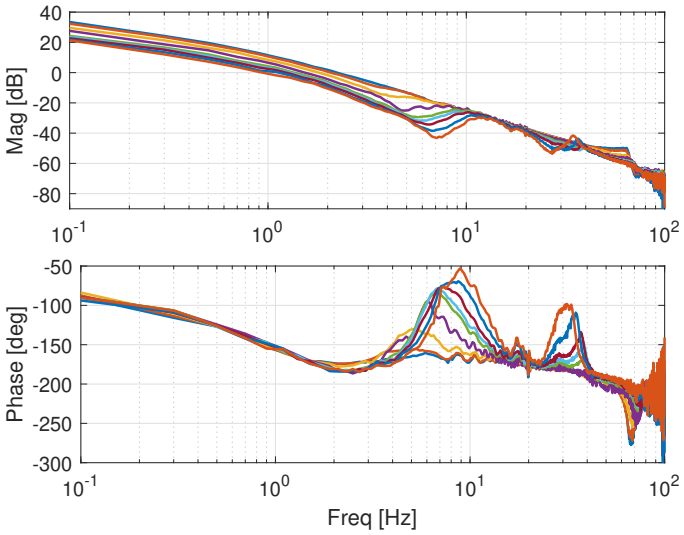

Fig. 6. Measured frequency response from motor torque to load angle for Joint 3, highlighting configuration-dependent variation in resonances and anti-resonance characteristics.

2) Conventional Controllers for Comparison: To benchmark performance, the proposed method is compared against two representative approaches. Case 1 is an $\mathcal{H}_\infty$ controller [7] designed using an identified parametric model, providing a model-based baseline with explicit frequency-domain performance guarantees. Case 2 is a heuristic FRF-based tuning approach derived from the original non-convex formulation in (17a)–(17f), where controller parameters are adjusted directly from FRF data but depend heavily on designer expertise and trial-and-error. For fairness, all controllers are implemented with the second-order structure ($qd = qn = 2$) and satisfy the performance and stability margin requirements described in Section III-A.

B. Frequency Response Data Acquisition

FRF data are obtained by applying multisine excitation signals from 0.1 Hz to 100 Hz to each joint and measuring the corresponding load-side angular responses. These measurements are then used to compute joint-level FRFs, as defined in (1). Fig. 6 shows representative FRFs from Joint 3, where resonance peaks (7–10 Hz and 30–40 Hz) arise from joint flexibility and configuration-dependent inertia, anti-resonance modes (4–7 Hz and 20–30 Hz) result from joint coupling and structural compliance.

These characteristics highlight a fundamental limitation of conventional model-based control: SISO parametric models can represent resonant modes but cannot capture anti-resonant modes in the relationship between motor torque and load angle [1]. In contrast, FRF measurements naturally reveal both resonance and anti-resonance phenomena. This capability to directly capture configuration-dependent dynamics

IEEE Robotics and Automation Letters (RA-L) paper, presented at ICRA 2026, Vienna, Austria. Cite as RA-L paper.

underscores the strength of the proposed data-driven approach, which mitigates unmodeled dynamics and parametric uncertainty.

C. Optimization Results for Controller Design

The proposed optimization method is applied to all joints using the measured FRF data. Joint-level controllers are synthesized to directly account for configuration-dependent dynamics following the optimization formulation in Sections III and IV. Results from Joint 3 are illustrated as representative due to similar behavior observed in other joints.

The controller order is set to a second-order numerator and denominator ($qn = qd = 2$), providing a simple yet sufficiently expressive structure for the considered system. Higher-order controllers can capture more dynamics but increase complexity and noise sensitivity, while lower-order controllers cannot capture the required dynamics. Thus, the second-order provides a practical balance between performance, complexity, and reproducibility.

As illustrated in Fig. 7(a), both Case 2 and the proposed method achieve higher sensitivity bandwidth compared to Case 1, which relies on an estimated parametric model. The proposed controller further outperforms Case 2 by explicitly optimizing the bandwidth parameter ζ. The complementary sensitivity in Fig. 7(b) demonstrates that the proposed method reduces overshoot amplification compared with both Case 1 and Case 2, while simultaneously increasing control bandwidth, thereby improving vibration suppression and tracking accuracy. Fig. 7(c) shows that the proposed controller intentionally allocates greater control effort at higher frequencies to expand bandwidth while satisfying the specified input constraints. The Nyquist plot in Fig. 8 confirms that all controllers satisfy the specified stability margins ($r_m = 0.5$, $\sigma = 1$) across varying configurations. These results validate that the proposed framework enables systematic, high-performance controller synthesis without the need for model identification or manual tuning.

D. Dynamic Evaluation on a High-Speed Drumming Task

1) Task Description: The proposed method is validated on a multi-joint coupled system using a drumming task, which involves fast motion, repeated impacts, and precise strikes, posing significant challenges for FJRs. In addition, the task introduces substantial configuration changes that induce large variations in link inertia, particularly in the upper joints. The combined effects of these dynamic variations and repeated impacts from drum strikes impose significant challenges on the controller.

As shown in Fig.9, the robot performs sequential strikes on four drums (D1→D2→D3→D4), executing two strikes per drum at a fixed tempo of 120 BPM. Each phase transition occurs within 0.4s, demanding accurate and fast response across configurations.

2) Tracking Performance and Impact Tolerance: Joint-space tracking results for all joints are shown in Fig. 10, ordered from top (Joint 1) to bottom (Joint 6). The task consists of four sequential phases, each involving two strikes, with

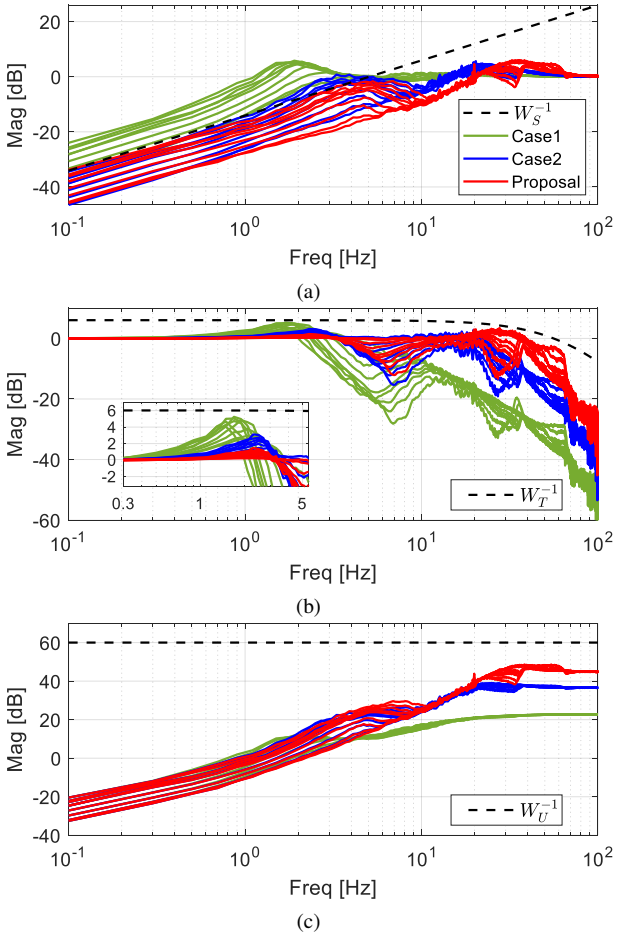

Fig. 7. Performance comparison for joint 3. (a) Sensitivity function, (b) Complementary sensitivity function, (c) Input sensitivity function.

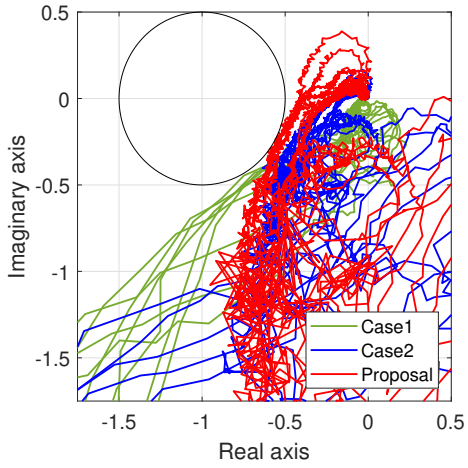

Fig. 8. Nyquist plot verifying the stability margin of the controllers with $r_m = 0.5$ and $\sigma = 1$.

phase transitions occurring every 0.4 s. The strike sequences are particularly evident in Joint 6 due to its distinct motion profile.

Substantial link inertia variation—particularly in joints 1 to 3—poses considerable control challenges. The reflected inertia in these joints changes dramatically throughout the task, which can significantly degrade control accuracy if not

IEEE Robotics and Automation Letters (RA-L) paper, presented at ICRA 2026, Vienna, Austria. Cite as RA-L paper.

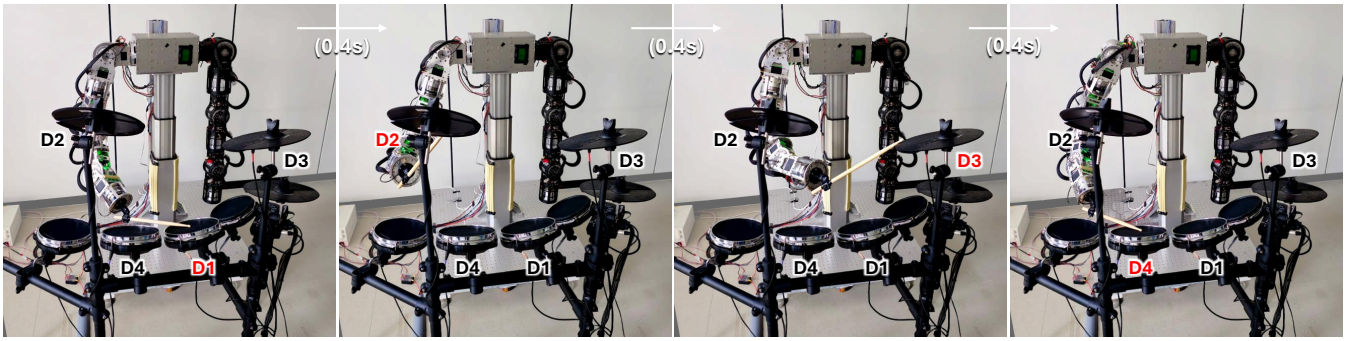

Fig. 9. Snapshots of the high-speed drumming task, showing the 7-DOF flexible joint robot executing four sequential strike phases (D1→D2→D3→D4) under large inertia variations and joint flexibility.

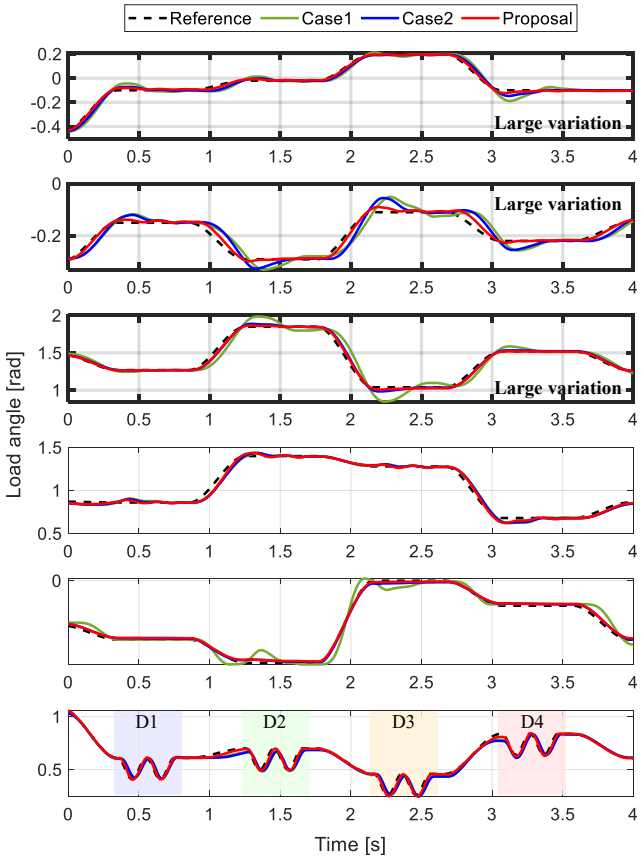

Fig. 10. Joint-space reference tracking during the high-speed drumming task for all joints (Joint 1–6, top to bottom). Each phase involves two strikes at 120 BPM with 0.4 s transitions. The proposed method achieves accurate tracking across varying configurations and repeated impacts.

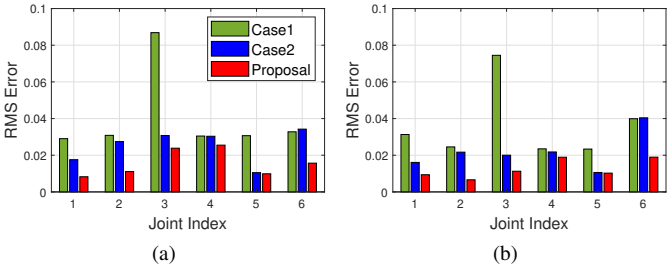

Fig. 11. Tracking error norms for all joints during the high-speed drumming task. (a) RMS error without impact (outside strike phases D1–D4), (b) RMS error with impact (within strike phases).

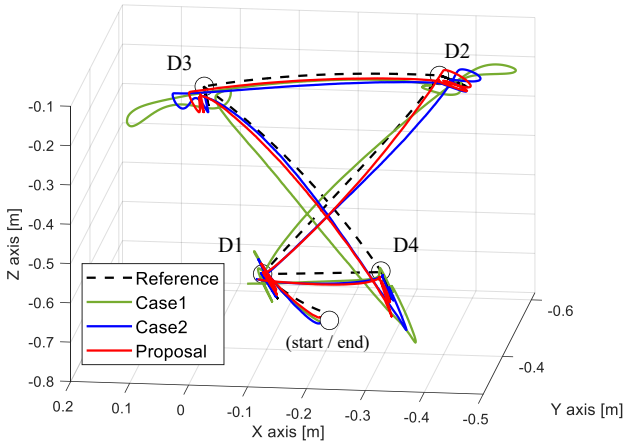

Fig. 12. End-effector trajectories in Cartesian space during the drumming task, illustrating tracking accuracy across multiple strike points.

properly compensated. This issue is evident in the performance of Case 1, which exhibits overshoot and reduced tracking precision due to limited bandwidth and sensitivity to modeling errors, as shown in Fig. 7.

In contrast, the proposed controller maintains consistent tracking performance across all joints by explicitly incorporating FRF data into the synthesis process. Overshoot is suppressed, and tracking errors are minimized even in the presence of multi-joint coupling, inertia variation, and repeated impacts. This observation is further supported by the tracking error norms in Fig. 11, where RMS errors are evaluated with and without impact occurring at the strike phases D1–D4. The proposed method consistently achieves the lowest errors in both cases, demonstrating robustness to impact disturbances.

Cartesian tracking accuracy is illustrated in Fig. 12, which shows the end-effector trajectory throughout the task. Case 1 exhibits substantial deviations at the strike points, reflecting limitations in control bandwidth. In contrast, the proposed controller maintains precise target alignment at each strike and reduces tracking errors during transitions, enabled by its enhanced bandwidth and robustness.

3) Acoustic Consistency Across Speed Variations: Acoustic analysis is conducted under two motion conditions during the drumming task: slow and fast phase transitions. As illustrated in Fig.9, the robot sequentially strikes four drums

IEEE Robotics and Automation Letters (RA-L) paper, presented at ICRA 2026, Vienna, Austria. Cite as RA-L paper.

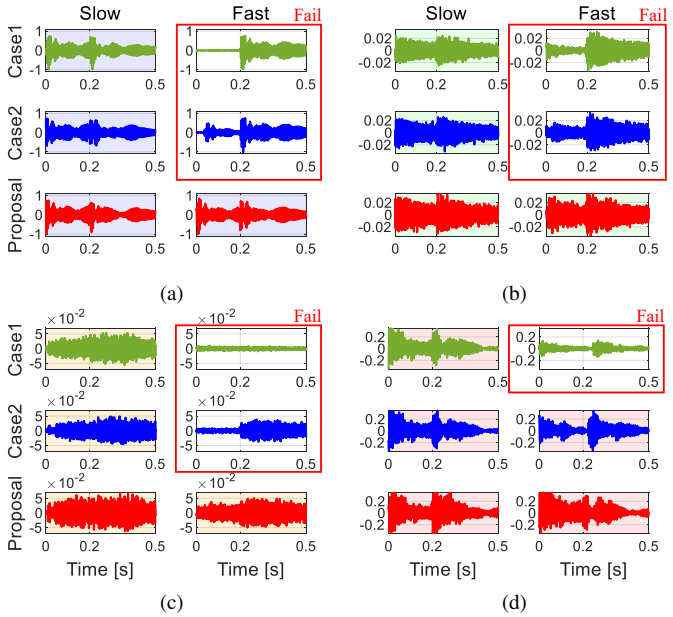

Fig. 13. Acoustic analysis of the drumming task under slow (1 s) and fast (0.4 s) phase transitions. (a)–(d) correspond to strike phases at D1–D4. The proposed method consistently produces two time-synchronized strikes per phase with matched amplitudes, whereas conventional methods exhibit inconsistent or missing strikes.

(D1→D2→D3→D4), performing two strikes per drum at a fixed tempo of 120 BPM. The phase transition duration is set to 1.0s for the slow-motion scenario and 0.4s for the fast-motion scenario. The fast-motion setting corresponds to the trajectory shown in Fig.10.

Fig.13 presents the resulting acoustic signals. The time axes for both scenarios are aligned, as the strike tempo remains constant. Case 1 and Case 2 fail to maintain acoustic consistency during fast transitions, producing mismatched sound patterns between the two strikes on each drum. These inconsistencies are highlighted by white background regions in the fast-motion plots, indicating deviations in waveform shape or peak amplitude. In contrast, colored regions denote consistent and repeatable acoustic output. Only the proposed method achieves identical acoustic signatures across both motion conditions, demonstrating its robustness to rapid transitions and dynamic disturbances.

VI. CONCLUSION

This paper presented a data-driven control optimization framework for flexible joint robots (FJRs) based on frequency response function (FRF) data. The proposed method eliminates the need for explicit model estimation by directly utilizing measured FRFs, and formulates controller synthesis as a convex optimization problem that maximizes control bandwidth while ensuring closed-loop stability across varying configurations. Experimental validation on a 7-DOF FJR demonstrated improved tracking accuracy, vibration suppression, and robustness relative to conventional approaches. The effectiveness of the proposed method was further confirmed through a high-speed drumming task, which imposed significant inertial variations and impact disturbances under rapid phase transitions.

Future work will explore the incorporation of multi-joint coupled FRF modeling to explicitly address joint interaction effects. Additionally, extending the framework to linear parameter-varying (LPV) synthesis will be investigated to further enhance adaptability under broader dynamic variations and operating conditions.

REFERENCES

[1] B. Siciliano, O. Khatib, and T. Kröger, *Springer handbook of robotics*. Springer, 2008, vol. 200.

[2] S. Haddadin, A. Albu-Schäffer, and G. Hirzinger, "Requirements for safe robots: Measurements, analysis and new insights," *The International Journal of Robotics Research*, vol. 28, no. 11-12, pp. 1507–1527, 2009.

[3] A. De Luca and W. J. Book, "Robots with flexible elements," in *Springer Handbook of Robotics*. Springer, 2016, pp. 243–282.

[4] L. Sun, W. Yin, M. Wang, and J. Liu, "Position control for flexible joint robot based on online gravity compensation with vibration suppression," *IEEE Trans. Ind. Electron.*, vol. 65, no. 6, pp. 4840–4848, 2017.

[5] S. Ozgoli and H. Taghirad, "A survey on the control of flexible joint robots," *Asian journal of control*, vol. 8, no. 4, pp. 332–344, 2006.

[6] C. Ott, A. Albu-Schaffer, A. Kugi, and G. Hirzinger, "On the passivity-based impedance control of flexible joint robots," *IEEE Transactions on Robotics*, vol. 24, no. 2, pp. 416–429, 2008.

[7] M. Makarov, M. Grossard, P. Rodriguez-Ayerbe, and D. Dumur, "Modeling and preview $\mathcal{H}_\infty$ control design for motion control of elastic-joint robots with uncertainties," *IEEE Transactions on Industrial Electronics*, vol. 63, no. 10, pp. 6429–6438, 2016.

[8] D. Lee, J. Back, and S. Oh, "Workspace nonlinear disturbance observer for robust position control of flexible joint robots," *IEEE Robotics and Automation Letters*, 2024.

[9] J. Swevers, W. Verdonck, and J. De Schutter, "Dynamic model identification for industrial robots," *IEEE control systems magazine*, vol. 27, no. 5, pp. 58–71, 2007.

[10] N. Paine, J. S. Mehling, J. Holley, N. A. Radford, G. Johnson, C.-L. Fok, and L. Sentis, "Actuator control for the nasa-jsc valkyrie humanoid robot: A decoupled dynamics approach for torque control of series elastic robots," *Journal of field robotics*, vol. 32, no. 3, pp. 378–396, 2015.

[11] R. van der Maas, A. van der Maas, R. Voorhoeve, and T. Oomen, "Accurate frf identification of lpv systems: nd-lpm with application to a medical x-ray system," *IEEE Transactions on Control Systems Technology*, vol. 25, no. 5, pp. 1724–1735, 2016.

[12] T. Bloemers, T. Oomen, and R. Tóth, "Frequency response data-based lpv controller synthesis applied to a control moment gyroscope," *IEEE IEEE Trans. Control Syst. Technol.*, vol. 30, no. 6, pp. 2734–2742, 2022.

[13] P. Schuchert and A. Karimi, "Frequency-domain data-driven position-dependent controller synthesis for cartesian robots," *IEEE Transactions on Control Systems Technology*, vol. 31, no. 4, pp. 1855–1866, 2023.

[14] X. Wang, W. Ohnishi, and T. Koseki, "Frequency response data based disturbance observer design: With application to a nonminimum phase motion stage," *IEEE/ASME Transactions on Mechatronics*, vol. 27, no. 6, pp. 5318–5326, 2022.

[15] H. Jung and S. Oh, "Data-driven optimization of integrated control framework for flexible motion control system," *IEEE Transactions on Industrial Informatics*, vol. 18, no. 7, pp. 4762–4772, 2021.

[16] K. Nakamura, K. Yubai, D. Yashiro, and S. Komada, "Controller design method achieving maximization of control bandwidth by using nyquist diagram," in *2016 International Automatic Control Conference (CACS)*. IEEE, 2016, pp. 35–40.

[17] S. Boyd, M. Hast, and K. J. ström, "Mimo pid tuning via iterated lmi restriction," *International Journal of Robust and Nonlinear Control*, vol. 26, no. 8, pp. 1718–1731, 2016.

[18] M. Hast, K. J. ström, B. Bernhardsson, and S. Boyd, "Pid design by convex-concave optimization," in *2013 European Control Conference (ECC)*. IEEE, 2013, pp. 4460–4465.

[19] D. Lee, K. Choi, J. Kim, W. Yun, T. Kim, K. Nam, and S. Oh, "Exsler: Development of a robotic arm for human skill learning," in *2023 IEEE/ASME International Conference on Advanced Intelligent Mechatronics (AIM)*. IEEE, 2023, pp. 209–214.